Near infrared fluorescent nanosensors for high spatiotemporal oxytocin imaging

Jaquesta A.M. Adams[1], Natsumi Komatsu[2], Nicole Navarro[1], Esther Leem[2], Xiaoqi Sun[2], Jiaxuan Zhao[3], Octavio I. Arias-Soto[1], and Markita P. Landry[2,4,5]

[1]University of California, Berkeley, Department of Chemistry, Berkeley, CA, USA.
[2]University of California, Berkeley, Department of Chemical and Biomolecular Engineering, Berkeley, CA, USA.
[3]University of California – Berkeley, Department of Molecular and Cellular Biology, Berkeley, CA, USA.
[4]California Institute for Quantitative Biosciences, QB3, University of California, Berkeley, CA, USA.
[5]Chan-Zuckerberg Biohub, San Francisco, CA, USA.
Correspondence to: landry@berkeley.edu

Abstract
Oxytocin is a neuropeptide thought to play a central role in regulating social and emotional behavior. Current techniques for neuropeptide imaging are generally limited in spatial and temporal resolution, real-time imaging capacity, selectivity for oxytocin over vasopressin, and application in young and non-model organisms. To avoid the use of endogenous oxytocin receptors for oxytocin probe development, we employed a protocol to evolve purely synthetic molecular recognition on the surface of near-infrared fluorescent single-walled carbon nanotubes (SWCNT) using single-stranded DNA (ssDNA). This probe reversibly undergoes up to a 172% fluorescence increase in response to oxytocin with a K_d of 4.93 µM. Furthermore, this probe responds selectively to oxytocin over oxytocin analogs, receptor agonists and antagonists, and most other neurochemicals. Lastly, we show our probe can image synaptic evoked oxytocin release in live mouse brain slices. Optical probes with the specificity and resolution requisite to image endogenous oxytocin signaling can advance the study of oxytocin neurotransmission for its role in both health and disease.

Introduction

Oxytocin is a nonapeptide primarily synthesized in the hypothalamus and known for its central role in regulating social and emotional behaviors. Alongside its receptor (OTR), oxytocin is widely distributed across the central and peripheral nervous systems and even across species. Historically, oxytocin was first recognized for its influence in reproductive actions such as lactation and uterine contraction but has since been implicated in behaviors such as recognition, pair and maternal bonding, non-reproductive social interactions, and anxiolysis (*1–5*). Consequently, dysfunction in oxytocin signaling has been implicated in the pathogenesis of neurological disorders related to social impairment such as schizophrenia, mood disorders, anxiety, and autism spectrum disorder (*6*, *7*). In fact, a significant area of study concerning oxytocin has investigated the therapeutic efficacy of exogenous oxytocin to treat such disorders (*8*). However, understanding the role of oxytocin in both health and disease remains incomplete owing to a lack of tools to directly probe oxytocin signaling at the spatiotemporal resolution requisite to elucidate oxytocinergic communication.

Existing tools to measure oxytocin include microdialysis which can be used to detect oxytocin in sampling fluids such as plasma or extracellular fluid. Following microdialysis sampling, oxytocin is quantified using an assay such as radioimmunoassay (RIA), enzyme immunoassay (EIA), or high-performance liquid chromatography (HPLC). Microdialysis coupled with an assay has been widely used to selectively measure oxytocin yet sampling typically occurs over minutes wherein sensitive samples may degrade and transient changes will not be captured

(*9*, *10*). By leveraging the redox active tyrosine, electrochemical methods can achieve rapid detection of oxytocin by leveraging the redox active tyrosine albeit with lower sensitivity relative to immunoassay-coupled microdialysis.(*11*) Recently, genetically encoded oxytocin sensing platforms have been reported for oxytocin (*12*, *13*). However, the timescale required for uniform expression of genetically encoded sensors may present a challenge in studying oxytocin release in non-model and young organisms, which is a key timepoint for the study of social development and disorders thereof. Furthermore, the use of GPCR receptors as sensing elements may affect endogenous G protein signaling pathways and can result in a lack of oxytocin selectivity in cases where the endogenous GPCR has affinity for multiple neuropeptides, as is the case for oxytocin and the closely related vasopressin. These features leave a need for real-time oxytocin imaging probes that can distinguish oxytocin from vasopressin and can be used irrespective of an organism's species and age. While several techniques have been developed in recent years to detect oxytocin their variable advantages and limitations make sensitive and selective monitoring of endogenous oxytocin dynamics an ongoing task and motivates the development of synthetic optical probes to add to the oxytocin interrogative toolkit.

To this end, we have utilized a synthetic molecular evolution method, systematic evolution of ssDNA ligands by exponential enrichment following adsorption to carbon nanotubes (SELEC) (*14*), to produce a sensitive and reversible oxytocin nanosensor capable of imaging oxytocin in the brain. The probe leverages the inherent tissue-transparent fluorescence of single-walled carbon nanotubes (SWCNT). SWCNT are biocompatible and photostable nanomaterials that can be functionalized with molecular recognition elements to develop sensors for targets of interest. As SWCNT photophysics is exciton-based, SWCNT fluorescence is modulated by the surrounding dielectric environment and, importantly, does not photobleach (*15*). Prior work has demonstrated the broad utility of noncovalent ssDNA-SWCNT as nanosensors for neurochemical imaging applications. For instance, $(GT)_6$-SWCNT (nIRCats) (*16*) have been used to image dopamine release in striatal brain tissue, and, more recently, at single dopamine release sites in neuronal soma and dendrites (*17*). SWCNT-based nanosensors have also been developed for neuromodulator serotonin (*14*, *18*). While SWCNT-based small-molecule neurotransmitters and neuromodulators have been successfully developed, it remained to be seen whether SWCNT-based neurochemical sensors could be developed for more structurally complex targets, such as neuropeptides. Here, we developed oxytocin-sensitive SWCNT-based probes using SELEC molecular recognition evolution, and identified a unique sequence of ssDNA that, when adsorbed to the surface of SWCNT, enables a strong fluorescence response towards oxytocin. The best-performing near-infrared oxytocin-selective (nIROT-SELEC) nanosensor responds to oxytocin with a change in fluorescence, $\Delta F/F_0$, of up to 1.72±0.01 in the nIR fluorescence emission window of 1000 to 1300 nm and is shown to bind reversibly to oxytocin with a K_d of 4.93±3.19 μM ($R_2 > 0.99$) in phosphate-buffered saline (PBS). We further demonstrate nIROT-SELEC selectivity for imaging oxytocin over analogs including vasopressin (VP), receptor agonists and antagonists, and other neurochemicals, motivating the use of nIROT-SELEC to image endogenous oxytocin signaling in brain tissue. As such, we show that nIROT-SELEC can be used to image electrically stimulated oxytocin release in acute brain tissue slices containing the paraventricular nucleus (PVN) and nucleus accumbens (NAc), suggesting that nIROT-SELEC can serve as a valuable tool to study neuropeptide signaling. In addition to providing a new tool for oxytocinergic neurobiology, our work here also confirms that molecular recognition can be evolved from purely synthetic elements. In prior work, we had shown that SELEC enables molecular recognition evolution for small molecule neuromodulator serotonin(*14*). In this work, we demonstrate the generalizability of the SELEC platform for evolving molecular recognition for larger and more structurally complex targets like oxytocin. With SELEC, we used a library of more than 10^{10} ssDNA-SWCNT conjugates to evolve for oxytocin selectivity through six rounds of amplifying oxytocin-selective ssDNA polymers, followed by deep sequencing to identify

unique polynucleotide sequences that provide oxytocin selectivity and sensitivity when surface adsorbed to SWCNT. ssDNA-SWCNT constructs generated from 6 successive rounds of evolution with oxytocin demonstrated improved sensitivity toward oxytocin compared to control constructs, ssDNA-SWCNT evolved in the absence of oxytocin.

Results

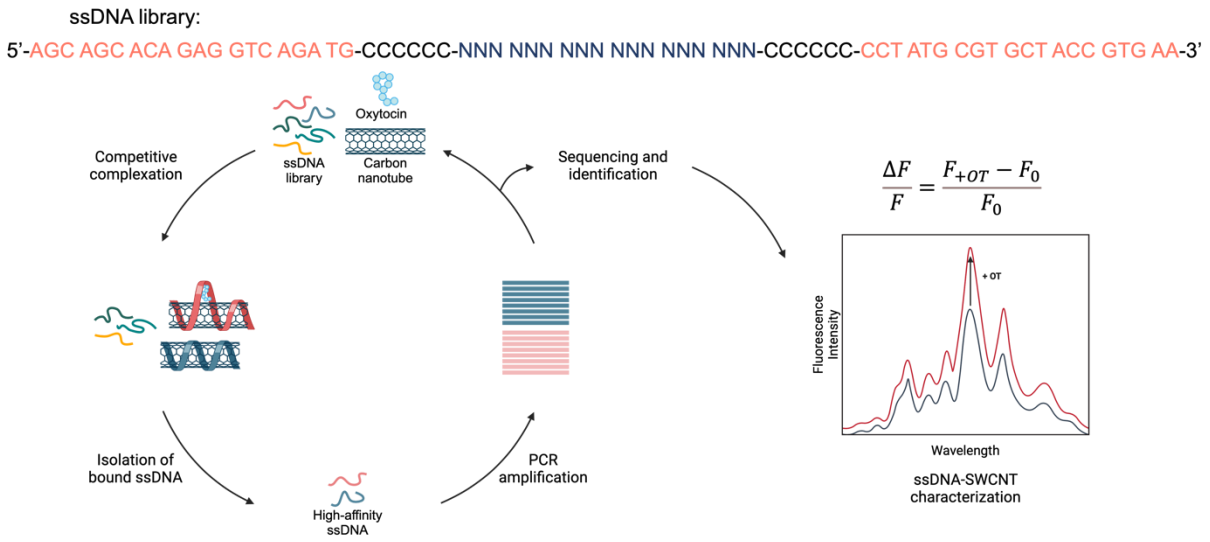

Figure 1. Schematic illustration of the SELEC nanosensor discovery process. In SELEC, SWCNTs are incubated with a ≥10-fold mass excess of ssDNA and 100 µM oxytocin (experimental library) or ssDNA only (control library). These mixtures are tip sonicated to generate a complex of either ssDNA-SWCNT bound to oxytocin (red) or ssDNA-SWCNT alone (blue). Unbound ssDNA are removed by spin-filtration and bound ssDNA are separated from SWCNT by thermal desorption to isolate high-affinity ssDNA. High-affinity ssDNA are then amplified by PCR and fed into the next selection round. Following six rounds, ssDNA selective for oxytocin when bound to SWCNT were identified by high-throughput sequencing and characterized by nIR spectroscopy. Created with BioRender.com.

SELEC identifies ssDNA-SWCNT constructs selective for neuropeptide oxytocin

We implemented SELEC to evolve ssDNA-SWCNT molecular recognition for oxytocin by designing our initial ssDNA library to be composed of greater than 10^{10} random 18-mer ssDNA sequences flanked by two C_6-mers and two 18-mer primer regions for polymerase chain reaction (PCR) amplification (Fig. 1). The PCR primers enabled enzymatic amplification and enrichment of high-affinity ssDNA aptamers. The purpose of the C_6 sequences was twofold: (1) the C_6 sequence has a high affinity for the carbon nanotube surface thus pinning the ssDNA sequences to the SWCNT and (2) the 6-mer sequences separate the random binding region of the ssDNA from the primer regions (*19*). Briefly, 10 µg of SWCNT was suspended using 100 nmol of the library of unique ssDNA sequences (200 µL, 0.5 mM), 100 nmol of oxytocin (100 µL, 1 mM), and 200 µL 20 mM acetate buffer to maintain a pH of 5 for oxytocin structural stability. An excess of ssDNA was used to promote competitive complexation of ssDNA to SWCNT in a manner that promotes oxytocin selectivity in the experimental library. Following competitive complexation, unbound ssDNA were removed by spin filtration. Bound ssDNA were subsequently desorbed, amplified by PCR, and isolated prior to use in subsequent rounds of SELEC. We previously determined that six rounds of SELEC is a sufficient threshold to observe neurochemical molecular recognition in the evolved library (*14*) and thus performed SELEC six times prior to

sequencing and characterization of the top oxytocin nanosensor candidates. ssDNA sequences from rounds 3-6 of SELEC were prepared and submitted for deep sequencing with an Illumina HiSeq 4000. A control sample was generated similarly but without an analyte as described previously (*14*). Control SELEC was used to identify ssDNA aptamers that only have a high affinity for the SWCNT surface, not the target analyte, or are subject to PCR biases (*20*). Sequencing analysis of the top oxytocin SELEC nanosensor candidates utilized only the 18-mer random region, excluding the polycytosine and PCR primer regions. *In vitro* and *ex vivo* characterization of the top candidates utilized the 18-mer random region and the C_6 regions to increase the density of molecular recognition sites on the SWCNT surface. Previous work demonstrated that nanosensors synthesized without the primer regions have increased sensitivity toward the target analyte.(*14*)

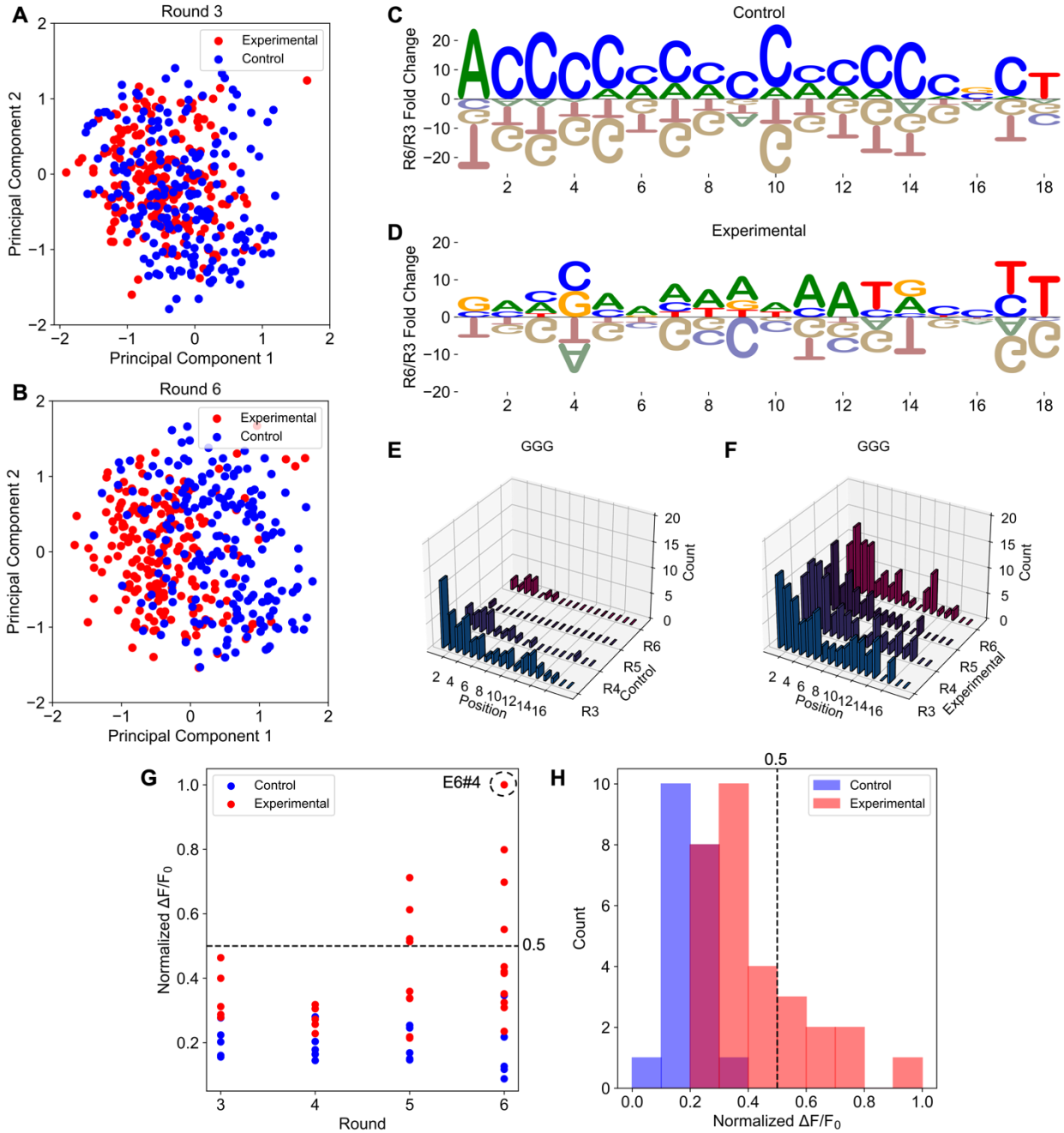

Figure 2. SELEC evolves ssDNA-SWCNT nanosensors for molecular recognition of oxytocin. (A) and **(B)** PCA plot for experimental (red) and control (blue) SELEC library sequences. Principal component analysis was performed for the top 200 ranked DNA sequences

from rounds 3 to 6 of the experimental and control SELEC libraries. Principal component 1 is plotted against principal component 2. **(C)** and **(D)** Fold change for each nucleotide at each position in the experimental library and control library from round 3 to round 6. **(E)** and **(F)** Trimer frequency of GGG at each nucleotide position for the experimental (left) and control (right) libraries across rounds 3 to 6. **(G)** Normalized $\Delta F/F_0$ upon 100 μM oxytocin addition to ssDNA-SWCNT constructs prepared from the top sequences across experimental and control rounds. Each point represents the average normalized $\Delta F/F_0$ of n = 3 measurements. The most sensitive nanosensor, E6#4, is circled. Data is visualized as a histogram in **(H).**

We identified the top 200 sequences from SELEC rounds 3 and 6 and analyzed them using principal component analysis (PCA) (Fig. 2A and B). Divergence of the experimental and control libraries was not observed in round 3 but was observed in round 6. This observation, attributable to the evolution of distinct nucleotide compositions, is likely resulting from the presence of oxytocin in SELEC during SELEC evolution, indicating the successful evolution of sequences for oxytocin molecular recognition. To further support this hypothesis, we calculated nucleotide fold change across the positions of the 18-mer random region from round 3 to round 6 in the experimental and control libraries (Fig. 2C and D). Key differences in nucleotide identity as a function of position along the ssDNA strand were identified between nucleotide enrichment in the experimental and control libraries. The control library demonstrated enrichment of cytosine at nearly every position except the first and final positions, as expected from prior literature demonstrating that cytosine is a tight-binding nucleotide for the SWCNT surface (*19*). However, in the experimental library, adenine was the most-enriched nucleotide overall, demonstrating preeminent fold change at positions 2 and 5-12. Furthermore, the experimental library generally demonstrated heterogeneity in nucleotide fold change across positions relative to the control library. Interestingly, both the experimental library and control library were most likely to contain adenine at position 1 and guanine at position 18 (Fig. S1), suggesting these trends at the outermost positions of the random region evolved to facilitate binding of the sequence to SWCNT rather than oxytocin.

We also analyzed the positional frequency of trimer appearance in the top 200 sequences of the experimental and control libraries. GGG was the most enriched trimer in the experimental library relative to the control library. GGG initially appeared in the top 20 trimers of the round 3 control library but declined in prevalence in the rounds that followed (Fig. 2E and F). Similarly, AGG and GGC were enriched across the experimental library and depleted in the control library, implicating these trimers in the evolution of oxytocin molecular recognition during SELEC (Fig. S2). Each of these trimers also displayed positional preference for the 5' end of the random recognition sequence.

GTG was the most abundant trimer across experimental rounds and the third-most abundant trimer across control rounds (Fig. S3). GTG also displayed positional preference with a strong enrichment on the 3’ end of the random recognition sequence. ACG and GCA were the only other trimers to appear in the top ten most abundant trimers in both the experimental and control libraries with GCA appearing at position 10 in both cases. The presence of these trimers in both the experimental and control libraries suggests that, while they may have a role in oxytocin molecular recognition, they may also be influential in SWCNT binding. The top 10 trimers evolved to recognize oxytocin in order of frequency, are presented in Table S1 and Table S2 for the experimental and control libraries, respectively.

Following nucleotide composition analysis of the SELEC libraries, we evaluated the sensitivity of ssDNA-SWCNT constructs prepared using the top enriched experimental and control library sequences per round. Sequences are identified as EN#M, where E represents experimental, N represents the SELEC round number (3-6), and M represents the sequence’s frequency ranking within said round (1-10). Correspondingly, control sequences are referred to as

CN#M. ssDNA-SWCNT nanosensors were prepared from the top 5 sequences of control SELEC rounds 3-6 and experimental SELEC rounds 3 and 4. The top ten sequences were selected for nanosensor synthesis from rounds 5 and 6 of experimental SELEC as sequences from these rounds were expected to have higher affinity for oxytocin than those from rounds 3 and 4 (Table S3).

ssDNA-SWCNT nanosensors were prepared by mixing ssDNA aptamer (100 µM, 1 mM in H_2O) with SWCNT (900 µL, 0.22 mg/mL in 1X PBS) and noncovalently adsorbing aptamers to the SWCNT surface by probe-tip sonication. All ssDNA sequences successfully suspended SWCNT. The candidate nanosensors were then diluted to 5 mg/L in PBS before fluorescence spectra were acquired (Fig. S4). Nanosensor optical response is reported as $\Delta F/F_0 = (F_t - F_0)/ F_0$, where F_0 is the baseline nanosensor fluorescence and F_t is the peak fluorescence after analyte incubation at timepoint *t*. Nanosensor response can be wavelength-dependent. Correspondingly, we observe the highest sensitivity to oxytocin at the peak corresponding to the 1195 nm wavelength and (8,6) chirality SWCNT, likely due to the 721 nm excitation wavelength used to acquire our spectra which excites the (8,6) chirality on-resonance (*21*, *22*). We therefore use this peak for all peak $\Delta F/F_0$ calculations.

The normalized fluorescence response of ssDNA-SWCNT nanosensors to 100 µM oxytocin was calculated for the selected top ssDNA sequences from the control and experimental libraries as a function of SELEC round (Fig. 2G). Fluorescence was normalized to the top responder in the experimental SELEC library, E6#4-SWCNT. Nanosensors prepared with control library sequences responded to oxytocin with a mean $\Delta F/F_0 = 0.19 \pm 0.06$, while those prepared with experimental library sequences responded to oxytocin with a mean $\Delta F/F_0 = 0.41 \pm 0.19$. The higher responsivity of nanosensors prepared with sequences from the experimental library compared to those from the control library indicates that these former sequences were successfully evolved via SELEC to bind oxytocin. Furthermore, all ssDNA-SWCNT constructs with a $\Delta F/F_0 > 0.5$ were identified through experimental SELEC rounds 5 and 6, with E6#4-SWCNT demonstrating the largest optical response to oxytocin [$\Delta F/F_0 = 1.05 \pm 0.04$ (mean ± SD); n = 3] (Fig. 2H). The increased appearance of high-responding sequences in experimental SELEC, particularly rounds 5 and 6, also supports that oxytocin sensitivity evolved as a function of SELEC round, as expected. As the most oxytocin-responsive nanosensor candidate, E6#4-SWCNT, was selected for further characterization as nIROT-SELEC (**n**ear-**I**nfra**R**ed **O**xy**T**ocin nanosensor identified by **SELEC**). The fluorescence intensity spectrum for nIROT-SELEC in response to oxytocin is shown in Fig. 3A.

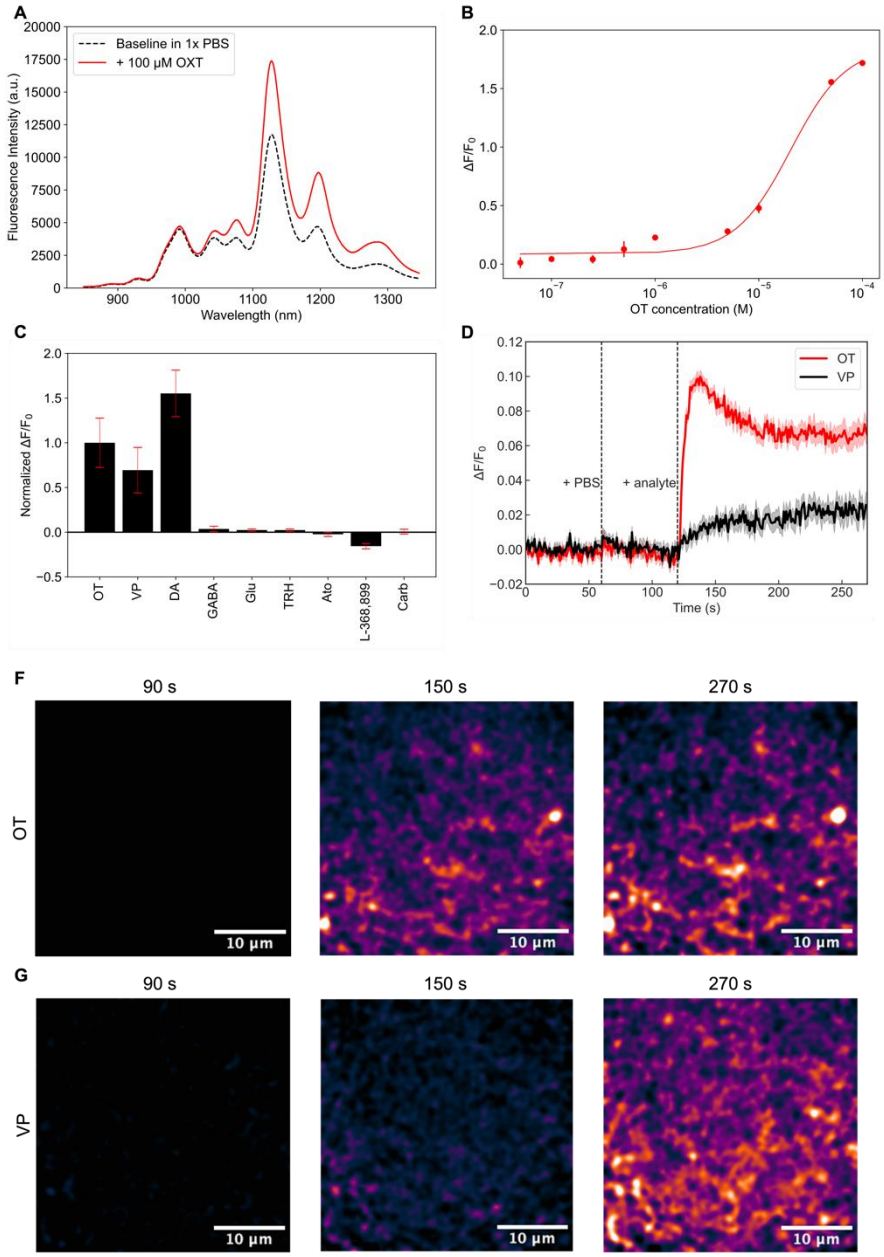

Figure 3. nIROT-SELEC demonstrates oxytocin sensitivity and selectivity. (A) Fluorescence intensity spectra for nIROT-SELEC before (black, dotted) and after (red) addition of 100 μM oxytocin. **(B)** Fluorescence modulation of nIROT-SELEC in response to oxytocin concentrations from 50 nM to 100 μM in PBS. **(C)** Response of nIROT-SELEC to 50 μM of oxytocin (OT) (n=15), vasopressin (VP) (n=6), dopamine (DA) (n = 3), y-aminobutyric acid (GABA) (n = 3), glutamate (Glu) (n = 3), thyrotropin hormone (TRH) (n = 3), atosiban (Ato) (n = 3), L-368,899 (n = 3), and carbetocin (Carb) (n = 3). Error bars are standard deviation. **(D)** Time-course integrated $\Delta F/F_0$ of immobilized nIROT-SELEC to 100 μM oxytocin (red line) and 100 μM vasopressin (black line). The shaded area is standard deviation. **(E)** nIR fluorescence images of immobilized nIROT-SELEC in the same field of view (left) 30 seconds following PBS addition, (center) 30 seconds following oxytocin addition, and (right) at the final timepoint. **(F)** nIR fluorescence images of immobilized nIROT-SELEC in the same field of view (left) 30 seconds following PBS addition, (center) 30 seconds following vasopressin addition, and (right) at the final timepoint. Scale bars represent 10 μm.

nIROT-SELEC demonstrates requisite sensitivity and selectivity for oxytocin imaging in brain tissue

We next characterized our nIROT-SELEC nanosensor for possible in-brain oxytocin imaging via *in vitro* characterization by spectroscopically measuring its response towards varying concentrations of oxytocin (Fig. 3B). nIROT-SELEC responded to 76-minute-long incubation with oxytocin in a concentration-dependent manner with nanomolar sensitivity. We next calculated nanosensor kinetic parameters by fitting nIROT-SELEC fluorescence response versus oxytocin concentration to a cooperative binding model (*23*). The equilibrium dissociation constant (K_d) was determined to be 4.93 ± 3.19 μM. To characterize nanosensor selectivity, nIROT-SELEC fluorescence modulation was evaluated for response to 50 μM concentrations of a panel of neurochemicals after 20 minutes, including vasopressin, dopamine, ɣ-aminobutyric acid (GABA), glutamate, and thyrotropin-releasing hormone (TRH) (Fig. 3C). nIROT-SELEC is selective against TRH [$\Delta F/F_0$ = 0.024 ± 0.013 (mean ± SD); n = 3], which is co-released in the hypothalamus alongside oxytocin. (*23*, *24*) As expected, nIROT-SELEC responds significantly to dopamine relative to oxytocin [$\Delta F/F_0$ = 1.55 ± 0.26 (mean ± SD); n = 3]. Nearly all ssDNA-SWCNT constructs demonstrate optical sensitivity to dopamine, necessitating that nIROT-SELEC is exclusively applied in nondopaminergic brain regions or that dopamine-suppressing pharmacology is implemented when probing dopaminergic regions. When using fluorescence spectroscopy, nIROT-SELEC is moderately sensitive to the oxytocin analog vasopressin relative to oxytocin [$\Delta F/F_0$ = 0.69 ± 0.25 (mean ± SD); n=6]. To further explore the selectivity of nIROT-SELEC for oxytocin over vasopressin in the imaging form factor in which its use is intended, we surface-immobilized nIROT-SELEC on a glass slide and imaged these surface-immobilized nanosensors prior to and following analyte addition (Fig. 3D, E, and F). Nanosensors were immobilized on MatTek glass-bottom microwell dishes (35 mm petri dish with 10 mm microwell). PBS was added after 60 s, and either oxytocin or vasopressin was added after 120 s. Following PBS addition, the average $\Delta F/F_0$ of 20 nanosensor regions of interest (ROIs) in a single field of view was -0.002 ± 0.003 (mean ± SD). When washed with oxytocin, the average $\Delta F/F_0$ of 10 ROIs in a single field of view was 0.091 ± 0.004 (mean ± SD) after 30 seconds. When washed with vasopressin, the average $\Delta F/F_0$ of 10 ROIs in a single field of view was only 0.012 ± 0.005 (mean ± SD) after 30 seconds, suggesting nIROT-SELEC has faster binding dynamics for oxytocin over vasopressin when immobilized. nIROT-SELEC maintained its fluorescence over continuous laser illumination over the course of the 270 second experiment without photobleaching, suggesting that nIROT-SELEC can bind and optically respond to oxytocin without signal attenuation on solid substrates. Importantly, these imaging results suggest that nIROT-SELEC demonstrates full selectivity for oxytocin over vasopressin when used for imaging experiments, enabling its use as an oxytocin nanosensor for brain neurochemical imaging.

Next, to explore nIROT-SELEC compatibility with pharmacology, the nanosensor's optical response was also tested for a response towards oxytocin receptor-targeting drugs. nIROT-SELEC fluorescence modulation was minimal upon treatment with oxytocin receptor agonists atosiban [$\Delta F/F_0$ = -0.023 ± 0.024 (mean ± SD); n = 3] and L-368,899 [$\Delta F/F_0$ = -0.16 ± 0.03 (mean ± SD); n = 3] , and oxytocin analog and receptor agonist, carbetocin [$\Delta F/F_0$ = 0.005 ± 0.027 (mean ± SD); n = 3]. These data suggest that our nanosensor can be leveraged to explore potential changes in oxytocin signaling induced by – and in conjunction with – pharmacological agents.

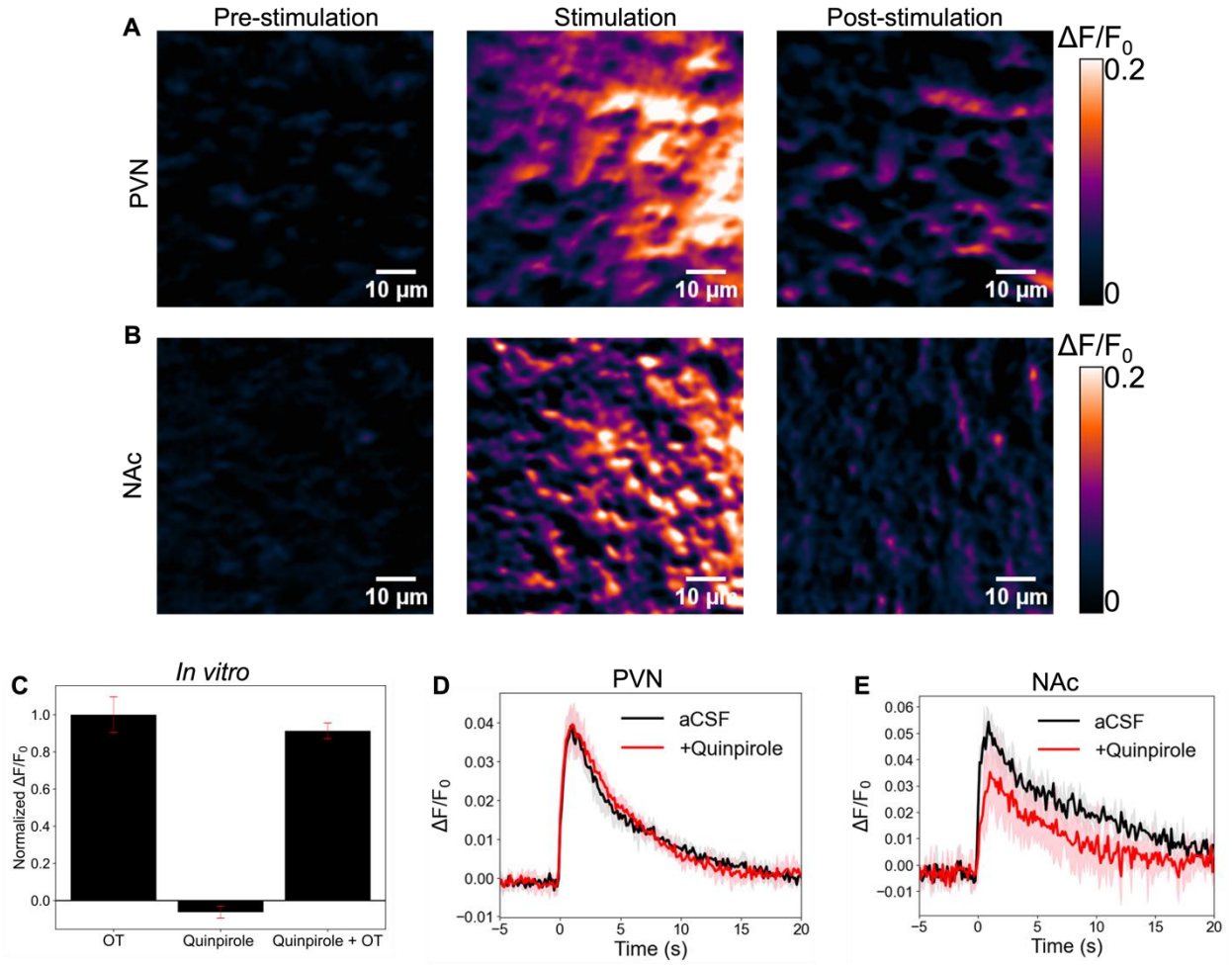

Figure 4. nIROT-SELEC detects neuromodulators *ex vivo*. (A) nIR fluorescence images of the paraventricular nucleus (PVN) in the same field of view following 0.5 mA electrical stimulation in standard aCSF. Three frames are represented for each: (left) "pre-stimulation" is the baseline nIROT-SELEC fluorescence before electrical stimulation, (center) "stimulation" is immediately following electrical stimulation, and (right) "post-stimulation" is after nIROT-SELEC fluorescence has returned to baseline. Scale bars represent 10 µm. **(B)** nIR fluorescence images of nucleus accumbens (NAc) in the same field of view following 0.5 mA electrical stimulation in standard aCSF. Three frames are represented for each: (left) "pre-stimulation" is the baseline nIROT-SELEC fluorescence before electrical stimulation, (center) "stimulation" is immediately following electrical stimulation, and (right) "post-stimulation" is after nIROT-SELEC fluorescence has returned to baseline. Scale bars represent 10 µm. **(C)** nIROT-SELEC response to oxytocin, quinpirole, and quinpirole + oxytocin *in vitro*. **(D)** Time-course integrated $\Delta F/F_0$ with (red) and without (black) 2 µM quinpirole addition in the PVN. The solid line (shadow) is the averaged (SD) value over three stimulation replicates. **(E)** Time-course integrated $\Delta F/F_0$ with (red) and without (black) 2 µM quinpirole addition in the NAc.

nIROT-SELEC enables imaging of electrically-evoked oxytocin release in acute brain slices

To explore the use of nIROT-SELEC for *ex vivo* oxytocin imaging, we imaged the nanosensor's fluorescence response in brain tissue with the extracellular space labeled with nIROT-SELEC. Acute coronal mouse brain slices of 300 µm thickness were prepared as previously described. (*24, 25*) Slices were incubated with 2 mg/L nIROT-SELEC in oxygen-saturated artificial cerebrospinal fluid (aCSF) for 15 min to enable sensors to diffuse into the brain tissue, resulting

in even and widespread SWCNT localization in the extracellular space (*16*, *26*). We subsequently rinsed the slices to remove excess nIROT-SELEC and transferred them to an aCSF-perfused chamber for 15 min before imaging. nIROT-SELEC-labeled slices were imaged by a custom-built nIR fluorescence upright epifluorescence microscope that excites nanosensors with 785 nm laser and obtains fluorescence from 900 to 1700 nm with an nIR camera with an imaging field of view measuring 175 µm by 140 µm.

We first investigated terminal release of oxytocin in the PVN, where oxytocin is synthesized and somatodendritically released (*27*, *28*). Applying a 0.5 mA current with a bipolar stimulating electrode evoked an instantaneous increase in nIROT-SELEC fluorescence [$\Delta F/F_0$ = 0.035 ± 0.007 (mean ± SD); n = 3] as shown in Fig. 4A. To verify their reversibility, we applied three repeated stimulations, 25 seconds apart to enable the tissue to recover. Each stimulation resulted in increased fluorescence [$\Delta F/F_0$ = 0.023 ± 0.008, 0.020 ± 0.006 and 0.019 ± 0.007 (means ± SD) for the 1st, 2nd, and 3rd stimulation, respectively; n = 2] (Fig. S5), demonstrating the nanosensor's reversibility. We next tested nIROT-SELEC nanosensors in a different brain region, NAc, because oxytocin signaling in the NAc is of great interest to elucidate social behaviors including bond formation (*29*) and social reward (*30*). Electrical stimulation of nIROT-SELEC labeled NAc tissue resulted in an immediate increase in nanosensor fluorescence intensity [$\Delta F/F_0$ = 0.042 ± 0.007 (means ± SD); n = 3] (Fig. 4B), confirming the utility of nIROT-SELEC to image oxytocin in multiple brain regions.

Since nIROT-SELEC responds to dopamine (Fig. 3C), to confirm the selectivity of oxytocin release in brain slice imaging experiments, we sought to bath-apply quinpirole, a D2 receptor agonist known to suppress dopamine release, into the brain slice imaging chamber. First, we conducted *in vitro* solution phase experiments (without biological tissue) to test the nIROT-SELEC fluorescent response towards quinpirole. Application of 2 µM quinpirole did not cause any fluorescent change to nIROT-SELEC [$\Delta F/F_0$ = -0.06 ± 0.03 (means ± SD); n = 3], confirming that it can be used to suppress dopamine release for selective oxytocin imaging in brain tissue (Fig. 4C). Furthermore, the nanosensor *in vitro* $\Delta F/F_0$ response to oxytocin was not altered by simultaneous application of 2 µM quinpirole [$\Delta F/F_0$ = 1.00 ± 0.10 for oxytocin only and $\Delta F/F_0$ = 0.91 ± 0.04 for oxytocin and quinpirole (means ± SD); P = 0.237; n = 3], confirming that nIROT-SELEC retained their functionality in the presence of D2 receptor agonist quinpirole (Fig. 4C). We next used 2 µM quinpirole to suppress any dopamine release in brain slices and compared nIROT-SELEC fluorescence response before and after quinpirole application. While quinpirole application did not cause a change in nanosensor fluorescence intensity when imaging in the PVN relative to quinpirole-free slice imaging [$\Delta F/F_0$ = 0.035 ± 0.007 in aCSF and $\Delta F/F_0$ = 0.034 ± 0.005 in aCSF and quinpirole (means ± SD); n = 3; P = 0.951] (Fig. 4D), quinpirole reduced the nanosensor fluorescence intensity by 42% in NAc [$\Delta F/F_0$ = 0.042 ± 0.007 in aCSF and $\Delta F/F_0$ = 0.024 ± 0.006 in aCSF and quinpirole (means ± SD); n = 3; P = 0.016] (Fig. 4E). This observation suggests we measure lower dopamine concentrations in PVN than those in NAc, agreeing with previous microdialysis analyses of oxytocin concentration in PVN (*31*, *32*) and in NAc (*33*–*35*). Furthermore, the number of oxytocin release sites, defined as regions of interest (ROIs) with high post-stimulation $\Delta F/F_0$, decreased by 22% in PVN [ROIs = 290 ± 30 in aCSF and ROIs = 225 ± 66 in aCSF and quinpirole (means ± SD); n = 3; P = 0.127] and by 40% in NAc [ROIs = 321 ± 59 in aCSF and ROIs = 193 ± 65 in aCSF and quinpirole (means ± SD); n = 3; P = 0.0988] (Fig. S6). Since release-site analysis is more sensitive than overall changes in nanosensor fluorescence (*36*), we predict that a small number of dopamine release sites are present in PVN, and a larger number of dopamine release sites are present in NAc, which are suppressed by quinpirole.

Discussion

Sensitive and selective high spatiotemporal imaging of neuropeptides is crucial to understanding the neurochemistry underpinning social behavior. Synthetic optical probes based

on carbon nanotubes offer a promising approach to imaging neuropeptide signaling with numerous advantages, including their inherent photostability, tissue transparency, reversibility of SWCNT fluorescence, compatibility with pharmacology, and species- and age-independent application. We have previously demonstrated the use of SELEC to achieve high-throughput selection of ssDNA-SWCNT nanosensors for small molecule neuromodulator serotonin detection. Here, we demonstrate application of SELEC to evolve molecular recognition for a larger, more complex neuropeptide target, oxytocin, and demonstrate the use of this sensor for oxytocin imaging in living brain tissue. From comparative analyses of SELEC experimental (performed in presence of oxytocin) and control (performed in absence of oxytocin) data, we first confirm that SELEC successfully evolves ssDNA sequences with oxytocin molecular recognition. Next, we characterize the nIR fluorescence response of ssDNA-SWCNT candidate nanosensors prepared from the top sequences in the control and experimental libraries across SELEC rounds. Together, these data demonstrate that SELEC can be used to achieve rapid identification of ssDNA-SWCNT nanosensors for both small-molecule and neuropeptide targets, potentiating the use of SELEC as a generic tool to evolve synthetic nanosensors for diverse biological imaging applications.

We identified a nanosensor, termed nIROT-SELEC, with a $\Delta F/F_0$ of 1.72±0.01 upon addition of 100 µM oxytocin. We showed that nIROT-SELEC has a K_d for oxytocin of 4.93±3.19 µM. Further, we demonstrated that nIROT-SELEC is selective for oxytocin over oxytocin analogs, receptor agonists and antagonists, and most other neurochemicals. Although nIROT-SELEC, similarly to most ssDNA-SWCNT, displayed a strong non-specific fluorescence modulation (normalized $\Delta F/F_0 = 1.55 \pm 0.26$) to dopamine, we demonstrate that quinpirole can be used to suppress dopamine release for selective oxytocin imaging in brain tissue. Application of quinpirole effectively suppressed dopamine release in *ex vivo* measurements (Fig. 4D and 4E), as the synthetic nature of nIROT-SELEC enables concurrent use of pharmacological agents during brain slice imaging. Furthermore, the unique cross-sensitivity of nIROT-SELEC for both oxytocin and dopamine can be used in the absence of dopamine suppressants to provide insights on the role and relative presence of both neuromodulators and the relative density of their release sites in tissue. In this work, we demonstrated the ability to do so by imaging oxytocin and dopamine release simultaneously, and next comparing these data to tissues exposed to D2 receptor agonists to calculate the relative contributions of dopamine, and dopamine release sites, in brain regions where both neuromodulators play a central neurobiological role. For example, the number of ROIs was 321 ± 59 (means ± SD) in NAc before quinpirole application and was reduced to 193 ± 65 (means ± SD) after quinpirole application (n = 3). The quinpirole-specific reduction in neuromodulator release sites (ROI = 128) can be attributed to endogenous dopamine release sites, and the release sites that persist in the presence of quinpirole (ROI = 193) correspond to oxytocin release, providing information on both neurochemicals with a single nanosensor. nIROT-SELEC could thus serve as an efficient platform to study the interplay between oxytocin and dopamine, which has become of great interest due to the hypothesized interplay of dopamine and oxytocin for maternal interaction, social reward, and pair-bond formation (*37–40*). nIROT-SELEC also responds moderately to vasopressin with a normalized $\Delta F/F_0 = 0.69 \pm 0.25$ over a 20-minute long solution-phase incubation, but immobilizing nIROT-SELEC provides selectivity for oxytocin over vasopressin. nIROT-SELEC also responds minimally to oxytocin receptor agonists and antagonists, indicating its potential to study the effects of receptor agonists and antagonists such as atosiban, carbetocin, and L-368,899 in the extracellular space.

Ultimately, our results suggest that nIROT-SELEC nanosensors offer a novel tool for high spatiotemporal fluorescence imaging to study oxytocin signaling in the brain, to elucidate the role of oxytocin in both health and disease.

Materials and Methods

Reagents

Small diameter HiPCo single-walled carbon nanotubes (SWCNT) were purchased from NanoIntegris. Oxytocin acetate salt hydrate, [Arg8]-vasopressin acetate salt, dopamine hydrochloride, thyrotropin-releasing hormone (TRH), glutamate, γ-aminobutyric acid, and atosiban were purchased from Millipore Sigma. Quinpirole and carbetocin were purchased from Tocris Bioscience. ssDNA sequences were purchased from Integrated DNA Technologies.

SELEC experimental protocol

The SELEC protocol was adapted from a previous paper.(*14*) The control sequence library from Jeong et al. was preserved. A new control sequence library (evolved in the absence of a target analyte) was thus not developed in this study.

The initial ssDNA library used for aptamer evolution consisted of 18 random nucleotides flanked by 1) two 6-mer polycytosines and 2) two 18-mer primer regions for polymerase chain reaction: AGCGTCGAATACCACTAC-C_6-N_{18}-C_6-GACCACGAGCTCCATTAG. During the first round of evolution, 100 nmol of the ssDNA library (200 μL, 0.5 mM) was mixed with pH 5 acetate buffer (200 μL, 20 mM) and 10 μg of SWCNT. The mixture was bath sonicated for 5 min, heated at 95ºC for 5 min to denature the ssDNA, then cooled to room temperature. Next, 100 μL of 1 mM oxytocin was added for a final volume of 500 μL. The mixture was allowed to incubate for 10 min at room temperature prior to probe tip sonication (Cole-Parmer Ultrasonic Processor, CPX130) with a 3 mm tip in ice-cold water for 20 min at 30% amplitude. The resulting suspension was centrifuged for 60 min at 16,000 g to pellet unsuspended SWCNT. The supernatant containing ssDNA-SWCNT and free ssDNA was collected and spin-filtered in a 0.5 mL 100 kDa MWCO Amicon Ultra cassette at 5,000 g for 2 min six times with DNAse-free water to remove unbound ssDNA. The suspension was then mixed with 0.1% (w/v) SDBS in 1X PBS (200 μL) and heated at 95ºC for 1 hr to detach bound ssDNA from the SWCNT surface. The suspension was then centrifuged for 60 min at 16,000 g to pellet aggregated SWCNT, and the supernatant containing ssDNA was collected. The solution was spin-filtered in a 0.5 mL 3 kDa MWCO Amicon Ultra cassette four times with DNAse-free water to remove SDBS.

The collected ssDNA was amplified by PCR, using a previously described protocol, with a FAM-modified forward primer (FAM-AGCGTCGAATACCACTAC) and biotinylated backward primer (biotin-CTAATGGAGCTCGTGGTC). The following PCR mixture was prepared for both preliminary and preparative PCR: Hot Start Taq DNA polymerase (2.75 U, New England Biolabs), 1X Hot Start Taq reaction buffer, forward primer (1 μM), backward primer (1 μM), deoxynucleotide triphosphate (500 μM), and ssDNA library template (~100 ng/mL). The total PCR mixture volume for each preliminary PCR reaction tube and preparative PCR well was 100 μL. DNAse-free water was added to achieve the desired volume. The following standard cycling conditions were used: initial denaturation for 900 s at 95ºC, *N* cycles of denaturation for 30 s at 95ºC, annealing for 30 s at 50ºC, and extension for 30 s at 72ºC, and final extension for 180 s at 72ºC.

Preliminary PCR was used to determine the number of PCR cycles (*N*) necessary to maximize dsDNA yield and minimize PCR by-product formation. Two PCR reaction tubes, with and without the ssDNA library template, were collected at the following cycles: 10, 15, 20, 25 and 30. A 4% agarose gel was prepared by heating 30 mL of 1X TBE buffer and 1.2 g of low range ultra agarose (Bio-Rad Laboratories) in a microwave oven and electrophoresis was performed on the preliminary PCR samples at 110 V for 18 min. The gel was stained with SYBR Gold, and the DNA bands were observed under UV light. The cycle number that yielded the brightest DNA band without nonspecific amplicons was selected for preparative PCR.

For preparative PCR, a 10 mL PCR mixture was prepared to produce a large quantity of ssDNA for the subsequent round of evolution. 100 μL of the PCR mixture was added to 95 of 96

reaction wells. A negative control well was prepared without the ssDNA library template. The preparative PCR product from a single reaction well was collected, purified with a GeneJet PCR purification kit (Thermo Scientific), and stored at -20ºC for sequencing preparation. The remaining preparative PCR product was spin-filtered using the 15 mL 10 kDa MWCO Amicon Ultra centrifugal filter.

To extract amplified ssDNA from the PCR product, 2.5 mL of Streptavidin-Sepharose beads (GE Healthcare) were first added to a mounted sintered Buchner funnel (<10 µm pore size). The beads were washed with 10 mL PBS buffer. PCR product was then incubated with beads for 30 min and passed through the funnel 3 times upon which the beads were washed again with 10 mL PBS. To elute and collect FAM-labeled ssDNA, 8 mL 0.2 M NaOH aqueous solution was added slowly to the beads. To desalt the ssDNA, an NAP-10 desalting column (GE Healthcare) was washed with deionized water (20 mL). 1 mL ssDNA solution was then added and drained. Upon the addition of 1.5 mL DNAse-free water, the eluate was collected. Desalted ssDNA was concentrated by spin-filtering in a 15 mL 3 kDa MWCO Amicon Ultra centrifugal filter and dried using a DNA Speedvac. For subsequent rounds of SELEC, the dried ssDNA was reconstituted in pH 5 acetate buffer, and the concentration was determined by measuring the absorbance at 260 nm.

High-throughput sequencing and analysis

To achieved multiplexed sequencing of SELEC libraries, two sequential PCR steps were used to add Illumina TruSeq universal adapter sequences and sequencing indices. Libraries from SELEC rounds 3 to 6 were sequenced with an Illumina HiSeq 4000 at the Genomic Sequencing Laboratory at the University of California, Berkeley. From the ~20 million raw sequences generated from each round, we discarded sequences that lacked the correct fixed regions (the 18-mer PCR primer regions and C_6 anchor regions). The FASTAptamer toolkit was used to filter and count sequence frequencies. All experiments in this manuscript used ssDNA sequences which excluded the 18-mer PCR primer regions. These sequences thus only contained the 18-mer random region flanked by the 6-mer polycytosine regions (i.e. C_6-N_{18}-C_6). Data visualizations of the top 200 sequences from the experimental and control SELEC libraries were performed using matplotlib and MATLAB.

Synthesis of ssDNA-SWCNT nanosensors

ssDNA-SWCNT nanosensors were prepared in a 1.5 mL DNA LoBind tube to a final volume of 1 mL by combining HiPCo SWCNT slurry (900 µL, 0.22 mg/mL in 1X PBS) and ssDNA (100 µL, 1 mM in H_2O). SWCNT slurry was vortexed for 3 sec and bath sonicated for 10 min prior to use. ssDNA were heated at 55°C for 5 min and cooled to room temperature before use. The mixture was vortexed for 3 sec, bath sonicated for 10 min, and probe-tip sonicated (Cole-Parmer Ultrasonic Processor, 3-mm tip) in ice-cold water for 10 min at 50% amplitude. The resulting suspensions were centrifuged at 16,000 g for 60 min to pellet unsuspended SWCNT. 900 µL of the supernatant was centrifuged again for 30 min. From this, 850 µL of the supernatant was carefully extracted and transferred to a new tube. Nanosensor concentration was calculated by measuring absorbance at 632 nm (NanoDrop One, Thermo Scientific) with an extinction coefficient of $\varepsilon = 0.036\ (\mathrm{mg/L})^{-1}\ \mathrm{cm}^{-1}$. Nanosensors were diluted to 5 mg/L in PBS for characterization experiments and were allowed to equilibrate at 4ºC for at least 24 hours prior to use in experiments.

Optical characterization of ssDNA-SWCNT nanosensors

Near-infrared fluorescence spectra were collected using a custom-built spectrometer and microscope as described previously(*41*). Measurements were obtained with a 20X objective on an inverted Zeiss microscope (Axio Observer.D1) coupled to a spectrometer (SCT 320, Princeton Instruments) and liquid nitrogen cooled InGaAs linear array detector (PyLoN-IR, Princeton Instruments). Nanosensor suspensions were excited with a 721 nm laser (OptoEngine LLC) inside

a polypropylene 384 well plate (Greiner Bio-One microplate). Spectra were collected with a 500 ms integration time.

For analyte screening, the baseline near-infrared fluorescence spectrum of each nanosensor-containing well was collected. PBS or analyte in PBS were added to wells, and fluorescence spectra were collected at regular time points until the maximum analyte fluorescence response was achieved (~20 min following addition). Responses were calculated and reported as $\Delta F/F_0 = (F_t - F_0)/ F_0$, where F_0 is the baseline nanosensor fluorescence and F_t is the peak fluorescence after analyte incubation at timepoint *t*. The peak fluorescence corresponds to the (8,6) SWCNT chirality, which has a maximum near-infrared fluorescence at ~1195 nm. To correct for variable fluctuations in the fluorescence measurement over time, the $\Delta F/F_0$ of the PBS control was subtracted from the analyte $\Delta F/F_0$.

Surface-immobilized nanosensors were imaged on an epifluorescence microscope (100X oil immersion objective) and a Ninox VIS-SWIR 640 camera (Raptor) and excited with a 721 nm laser. For each imaging experiment, 120 µL PBS was added and the z-plane was refocused prior to recording. Image stacks were collected with a 950 ms exposure time and 1 Hz frame rate for 270 seconds and total frames.

For immobilization experiments, nanosensors were immobilized on MatTek glass-bottom microwell dishes (35 mm petri dish with 10 mm microwell). The dish was washed twice with 1X PBS (150 µL), 15 mg/L nanosensors (100 µL, in PBS) were added, incubated for 30 min, and removed, then the dish was washed twice again with 1X PBS (150 µL). For imaging immobilized SWCNT, PBS was added at frame 60 and analyte was added at frame 120.

Image stacks were processed in ImageJ by applying a median filter (2.0-pixel radius) and gaussian filter (2.0-pixel radius). ROI analysis was automated using a Python script. ROI size was set to 25x25 pixels. Responses were calculated as $\Delta F/F_0 = (F_f - F_0)/ F_0$ for each ROI, where F_0 was the mean integrated fluorescence across the ROI at frame 1 and F_f was the mean integrated fluorescence for frame *f*, where *f* = 1-300. To account for microscope drift, slope was calculated from frame 1 to frame 110 using the sklearn.linear_model Linear Regression function and used to determine and subtract drift from the overall integrated fluorescence. $\Delta F/F_0$ for the top 10 ROIs (ranked by response at *f* = 300) were averaged and presented with standard deviation.

Acute slice preparation and nanosensor labeling

C57BL/6 strain male mice were purchased from Jackson Laboratory (stock no. 000664) and were 14-17 weeks old when imaged. The mice were weaned on postnatal day 21, and group-housed with nesting material on a 12:12 light cycle. All animal procedures were approved by the UC Berkeley Animal Care and Use Committee (ACUC).

Acute brain slices were prepared following the protocols described in Ref. (*24*, *25*). Cutting buffer (119 mM NaCl, 26.2 mM $NaHCO_3$, 2.5 mM KCl, 1mM NaH_2PO_4, 3.5 mM MgCl4, 10 mM glucose, all purchased from Sigma-Aldrich) and aCSF (119 mM NaCl, 26.2 mM $NaHCO_3$, 2.5 mM KCl, 1mM NaH_2PO_4, 1.3 mM $MgCl_2$, 10 mM glucose, 2 mM $CaCl_2$, all purchased from Sigma-Aldrich) were prepared and bubbled with carbogen gas (oxygen/carbon dioxide 95% O_2, 5% CO_2, Praxair, cat. no. BIOXCD5C-K). The animals were deeply anesthetized via intraperitoneal injection of ketamine (120 mg/kg) and xylazine (24 mg/kg) and transcardially perfused with 5 mL of ice-cold cutting buffer. The brain was subsequently extracted, mounted on a vibratome cutting stage (Leica VT 1000) in the carbogen-bubbled cutting buffer, and cut into 300 µm thick coronal slices with microtome razor blades (Personna, double edge super blades; VWR, cat. no. 100491-888). Slices were incubated at 37°C for 30 min in oxygen saturated aCSF in a chamber (Scientific Systems Design, Inc., BSK4) and then transferred to room temperature for 30 min. To label the slice with nanosensors, slices were transferred to a separate incubation chamber (Scientific Systems Design, Inc., BSK2) filled with 5 mL of carbogen-bubbled aCSF at room temperature. Nanosensors were applied to the surface of brain slices with a pipette to a final

concentration of 2 mg/L and incubated for 15 min. Slices were rinsed for 5 sec with bubbled aCSF through 3 wells of a 24-well plate to remove unlocalized nanosensors, transferred back to the main chamber, and rested for at least 15 min before imaging.

nIR Microscope Design

A home-built upright epifluorescent microscope (Olympus, Sutter Instruments) was used to image fluorescent response on nanosensors embedded in acute brain slices. 785-nm CW diode laser (OptoEngine LLC, MDL-III-785R-300mW) was used for excitation. After passing through a custom fluorescence filter cube [excitation: 800 nm shortpass (Thorlabs, FESH0800), dichroic: 900 longpass (Thorlabs, DMLP990R), and emission: 900 longpass (Thorlabs, FELH0900)], the beam reaches sample via a 60X objective (Nikon, CFI Apochromat NIR 60X W). Fluorescnece was collected with a two-dimensional InGaAs array detector (Raptor Photonics, Ninox 640). Microscope operation was controlled by Micro-Manager Open Source Microscopy Software (*42*).

Electrical stimulation evoked neurochemical imaging with nIR microscope

Carbogen-bubbled aCSF was flew through the microscope chamber with a perfusion pump (World Precision Instruments, Peri-Star Pro) and an aspirator pump (Warner Instruments, Dedicated Workstation Vacuum System) at 2 mL/min. Temperature of the imaging chamber's temperature was kept at 32°C with an inline heater with feedback control (Warner Instruments, TV-324C). Slices labeled with nanosensors were placed in the chamber with a Tissue harp (Warner Instruments), and a bipolar stimulation electrode (MicroProbes for Life Science Stereotrodes Platinum/Iridium Standard Tip) was positioned to the targeted field of view, which was adjusted with a 4X objective (Olympus XLFluor 4X/340) followed by a 60X objective and was at least 10 µm away from the stimulation electrode. Using Micro-Manager, nIR fluorescent images were acquired at frame rates of 8 frames/s (nominal) for 600 frames, where 1 millisecond of 0.5 mA stimulation was applied at after 200 frames of baseline. This image acquisition was repeated three times with the same field of view, with 5 min of waiting time in between. Subsequently 2 µM of quinpirole (Fisher Scientific, 10-611-0) was applied to the chamber through aCSF perfusion and slices were incubated for 15 min before imaging. Images were acquired in the same field of view as the one before quinpirole applications for three times with 5 min between each stimulation.

Image processing and data analysis of nanosensor fluorescence response

Imaging movie files were processed using a custom MATLAB application (https://github.com/jtdbod/Nanosensor-Brain-Imaging) or Python code (https://github.com/NicholasOuassil/NanoImgPro) (schematically summarized in Fig. S7). Integrated $\Delta F/F_0$ ($\Delta F/F_0$ for the entire field of view, 175 µm by 140 µm) (Fig. 4D, E, S7A and S7D) was calculated as $\Delta F/F_0 = (F- F_0) /F_0$, where F_0 is the average intensity for the first 5% of frames and F is the dynamic fluorescence intensity from the entire field of view (Fig. S7B) and averaged over three stimulation replicates. Next, a 25x25 pixel (corresponding to 6.8 µm by 6.8 µm) grid mask was applied to the image stack to minimize bias and improve stack processing time, and then a median filter convolution within each grid was calculated. For each grid square $\Delta F/F$ was calculated, and they were identified as regions of interest (ROI) if the F around time of stimulation (200 frames) is 3 standard deviations above the baseline F_0 activity (Fig. S7E). Subsequently, the number of ROIs identified from three stimulation replicates were averaged to give the slice average hotspot number (Fig. S6B and S6E). Lastly, $\Delta F/F_0$ was averaged over all identified ROIs, corresponding to the average image stack peak $\Delta F/F_0$ (Fig. S7F). The average image stack peak $\Delta F/F$ from the three stimulation replicates were then average to give the slice mean peak $\Delta F/F_0$ (Fig. S6C and S6F). $\Delta F/F_0$ for the entire field of view can also be obtained by applying a 640x640 pixel to the Python code above.

References

1. B. Jurek, I. D. Neumann, The Oxytocin Receptor: From Intracellular Signaling to Behavior. *Physiological Reviews* **98**, 1805–1908 (2018).
2. Z. R. Donaldson, L. J. Young, Oxytocin, Vasopressin, and the Neurogenetics of Sociality. *Science* **322**, 900–904 (2008).
3. J. T. Winslow, T. R. Insel, Neuroendocrine basis of social recognition. *Curr Opin Neurobiol* **14**, 248–253 (2004).
4. L. J. Young, Z. Wang, The neurobiology of pair bonding. *Nat Neurosci* **7**, 1048–1054 (2004).
5. M. Yoshida, Y. Takayanagi, K. Inoue, T. Kimura, L. J. Young, T. Onaka, K. Nishimori, Evidence That Oxytocin Exerts Anxiolytic Effects via Oxytocin Receptor Expressed in Serotonergic Neurons in Mice. *J. Neurosci.* **29**, 2259–2271 (2009).
6. P. Kirsch, Oxytocin in the socioemotional brain: implications for psychiatric disorders. *Dialogues in Clinical Neuroscience* **17**, 463 (2015).
7. S. Yoon, Y.-K. Kim, Possible oxytocin-related biomarkers in anxiety and mood disorders. *Prog Neuropsychopharmacol Biol Psychiatry* **116**, 110531 (2022).
8. L. Peled-Avron, A. Abu-Akel, S. Shamay-Tsoory, Exogenous effects of oxytocin in five psychiatric disorders: a systematic review, meta-analyses and a personalized approach through the lens of the social salience hypothesis. *Neuroscience & Biobehavioral Reviews* **114**, 70–95 (2020).
9. A. Inutsuka, D. Ino, T. Onaka, Detection of neuropeptides in vivo and open questions for current and upcoming fluorescent sensors for neuropeptides. *Peptides* **136**, 170456 (2021).
10. V. I. Chefer, A. C. Thompson, A. Zapata, T. S. Shippenberg, Overview of Brain Microdialysis. *Current Protocols in Neuroscience* **47** (2009).
11. K. Asai, T. A. Ivandini, Y. Einaga, Continuous and selective measurement of oxytocin and vasopressin using boron-doped diamond electrodes. *Sci Rep* **6**, 32429 (2016).
12. S. Valtcheva, H. A. Issa, C. J. Bair-Marshall, K. A. Martin, K. Jung, Y. Zhang, H.-B. Kwon, R. C. Froemke, Neural circuitry for maternal oxytocin release induced by infant cries. *Nature* **621**, 788–795 (2023).
13. T. Qian, H. Wang, P. Wang, L. Geng, L. Mei, T. Osakada, L. Wang, Y. Tang, A. Kania, V. Grinevich, R. Stoop, D. Lin, M. Luo, Y. Li, A genetically encoded sensor measures temporal oxytocin release from different neuronal compartments. *Nat Biotechnol* **41**, 944–957 (2023).
14. S. Jeong, D. Yang, A. G. Beyene, J. T. Del Bonis-O'Donnell, A. M. M. Gest, N. Navarro, X. Sun, M. P. Landry, High-throughput evolution of near-infrared serotonin nanosensors. *Science Advances* **5**, eaay3771 (2019).
15. D. A. Heller, S. Baik, T. E. Eurell, M. S. Strano, Single-Walled Carbon Nanotube Spectroscopy in Live Cells: Towards Long-Term Labels and Optical Sensors. *Advanced Materials* **17**, 2793–2799 (2005).
16. A. G. Beyene, K. Delevich, J. T. D. Bonis-O'Donnell, D. J. Piekarski, W. C. Lin, A. W. Thomas, S. J. Yang, P. Kosillo, D. Yang, G. S. Prounis, L. Wilbrecht, M. P. Landry, Imaging striatal dopamine release using a nongenetically encoded near infrared fluorescent catecholamine nanosensor. *Science Advances* **5**, eaaw3108–eaaw3108 (2019).
17. C. Bulumulla, A. T. Krasley, B. Cristofori-Armstrong, W. C. Valinsky, D. Walpita, D. Ackerman, D. E. Clapham, A. G. Beyene, Visualizing synaptic dopamine efflux with a 2D composite nanofilm. *Elife* **11**, e78773 (2022).
18. M. Dinarvand, E. Neubert, D. Meyer, G. Selvaggio, F. A. Mann, L. Erpenbeck, S. Kruss, Near-Infrared Imaging of Serotonin Release from Cells with Fluorescent Nanosensors. *Nano Lett.* **19**, 6604–6611 (2019).
19. M. P. Landry, L. Vuković, S. Kruss, G. Bisker, A. M. Landry, S. Islam, R. Jain, K. Schulten, M. S. Strano, Comparative Dynamics and Sequence Dependence of DNA and RNA

Binding to Single Walled Carbon Nanotubes. *J Phys Chem C Nanomater Interfaces* **119**, 10048–10058 (2015).
20. S. G. Acinas, R. Sarma-Rupavtarm, V. Klepac-Ceraj, M. F. Polz, PCR-Induced Sequence Artifacts and Bias: Insights from Comparison of Two 16S rRNA Clone Libraries Constructed from the Same Sample. *Appl Environ Microbiol* **71**, 8966–8969 (2005).
21. X. Tu, S. Manohar, A. Jagota, M. Zheng, DNA sequence motifs for structure-specific recognition and separation of carbon nanotubes. *Nature* **460**, 250–253 (2009).
22. S. Nanot, N. A. Thompson, J.-H. Kim, X. Wang, W. D. Rice, E. H. Hároz, Y. Ganesan, C. L. Pint, J. Kono, "Single-Walled Carbon Nanotubes" in *Springer Handbook of Nanomaterials* (Springer, Berlin, Heidelberg, 2013; https://link.springer.com/chapter/10.1007/978-3-642-20595-8_4), pp. 105–146.
23. R. L. Pinals, F. Ledesma, D. Yang, N. Navarro, S. Jeong, J. E. Pak, L. Kuo, Y.-C. Chuang, Y.-W. Cheng, H.-Y. Sun, M. P. Landry, Rapid SARS-CoV-2 Spike Protein Detection by Carbon Nanotube-Based Near-Infrared Nanosensors. *Nano Lett.* **21**, 2272–2280 (2021).
24. D. J. Piekarski, J. R. Boivin, L. Wilbrecht, Ovarian Hormones Organize the Maturation of Inhibitory Neurotransmission in the Frontal Cortex at Puberty Onset in Female Mice. *Curr Biol* **27**, 1735-1745.e3 (2017).
25. S. J. Yang, J. T. D. Bonis-O'Donnell, A. G. Beyene, M. P. Landry, Near-infrared catecholamine nanosensors for high spatiotemporal dopamine imaging. *Nat Protoc* **16**, 3026–3048 (2021).
26. A. G. Godin, J. A. Varela, Z. Gao, N. Danné, J. P. Dupuis, B. Lounis, L. Groc, L. Cognet, Single-nanotube tracking reveals the nanoscale organization of the extracellular space in the live brain. *Nat Nanotechnol* **12**, 238–243 (2017).
27. L. Young, "Oxytocin: Synthesis, Secretion and Reproductive Functions. Knobil and Neill, Physiology of Reproduction." (2006).
28. R. C. Froemke, L. J. Young, Oxytocin, Neural Plasticity, and Social Behavior. *Annu Rev Neurosci* **44**, 359–381 (2021).
29. L. J. Young, M. M. Lim, B. Gingrich, T. R. Insel, Cellular Mechanisms of Social Attachment. *Hormones and Behavior* **40**, 133–138 (2001).
30. G. Dölen, A. Darvishzadeh, K. W. Huang, R. C. Malenka, Social reward requires coordinated activity of nucleus accumbens oxytocin and serotonin. *Nature* **501**, 179–184 (2013).
31. M. R. Melis, S. Succu, M. S. Mascia, L. Cortis, A. Argiolas, Extra-cellular dopamine increases in the paraventricular nucleus of male rats during sexual activity. *European Journal of Neuroscience* **17**, 1266–1272 (2003).
32. K. M. Kendrick, Microdialysis measurement of in vivo neuropeptide release. *Journal of Neuroscience Methods* **34**, 35–46 (1990).
33. L. H. Parsons, J. B. Justice Jr., Extracellular Concentration and In Vivo Recovery of Dopamine in the Nucleus Accumbens Using Microdialysis. *Journal of Neurochemistry* **58**, 212–218 (1992).
34. H. O. Pettit, J. B. Justice, Dopamine in the nucleus accumbens during cocaine self-administration as studied by in vivo microdialysis. *Pharmacology Biochemistry and Behavior* **34**, 899–904 (1989).
35. L. H. Parsons, J. B. Justice, Perfusate serotonin increases extracellular dopamine in the nucleus accumbens as measured by in vivo microdialysis. *Brain Research* **606**, 195–199 (1993).
36. S. J. Yang, J. T. del B. O'Donnell, F. Giordani, J. Wang, A. Lui, D. Piekarski, A. Irrinki, D. V. Schaffer, M. P. Landry, Synaptic scale dopamine disruption in Huntington's Disease model mice imaged with near infrared catecholamine nanosensors. bioRxiv [Preprint] (2022). https://doi.org/10.1101/2022.09.19.508617.
37. M. Numan, L. J. Young, Neural mechanisms of mother-infant bonding and pair bonding: Similarities, differences, and broader implications. *Horm Behav* **77**, 98–112 (2016).

38. Y. Liu, Z. X. Wang, Nucleus accumbens oxytocin and dopamine interact to regulate pair bond formation in female prairie voles. *Neuroscience* **121**, 537–544 (2003).
39. L. Xiao, M. F. Priest, J. Nasenbeny, T. Lu, Y. Kozorovitskiy, Biased Oxytocinergic Modulation of Midbrain Dopamine Systems. *Neuron* **95**, 368-384.e5 (2017).
40. L. W. Hung, S. Neuner, J. S. Polepalli, K. T. Beier, M. Wright, J. J. Walsh, E. M. Lewis, L. Luo, K. Deisseroth, G. Dölen, R. C. Malenka, Gating of social reward by oxytocin in the ventral tegmental area. *Science* **357**, 1406–1411 (2017).
41. A. G. Beyene, G. S. Demirer, M. P. Landry, Nanoparticle-Templated Molecular Recognition Platforms for Detection of Biological Analytes. *Curr Protoc Chem Biol* **8**, 197–223 (2016).
42. A. D. Edelstein, M. A. Tsuchida, N. Amodaj, H. Pinkard, R. D. Vale, N. Stuurman, Advanced methods of microscope control using μManager software. *J Biol Methods* **1**, e10 (2014).

Acknowledgments

Funding: J.A.M.A. acknowledges the support of the HHMI Gilliam Fellowship program and the NSF Graduate Research Fellowship program. N.K. acknowledges support by the Schmidt Science Fellows program, in partnership with the Rhodes Trust. This work was supported by NIH S10 OD018174 Instrumentation Grant. M.P.L acknowledges support of a Burroughs Wellcome Fund Career Award at the Scientific Interface (CASI), a Dreyfus foundation award, the Philomathia foundation, an NIH MIRA award R35GM128922, an NIH R21 NIDA award 1R03DA052810, an NSF CAREER award 2046159, an NSF CBET award 1733575, a CZI imaging award, a Sloan Foundation Award, a McKnight Foundation award, a Simons Foundation Award, a Moore Foundation Award, and a Schmidt Foundation Award. M.P.L is a Chan Zuckerberg Biohub investigator, and a Hellen Wills Neuroscience Institute Investigator. **Author contributions:** N.N. performed the iterative process of SELEC. N.N. and J.A.M.A. analyzed the high-throughput sequencing data. N.N., J.A.M.A., X.S., E.L., and O.I.A.S characterized the nanosensors *in vitro*. N.K. and J.Z. performed the *ex vivo* experiments. J.A.M.A., N.K., N.N. and M.P.L. wrote the manuscript. All authors discussed the results and commented on the manuscript. **Competing interests:** The authors declare that they have no competing interests. **Data and materials availability:** All data needed to evaluate the conclusions in the paper are present in the paper and the Supplementary Information. Additional data related to this paper may be requested from the authors.